

Nematic superconductivity from selective orbital pairing in $\text{Ba}(\text{Fe}_{1-x}\text{M}_x)_2\text{As}_2$ ($\text{M} = \text{Co}, \text{Ni}$) single crystals

Mason Klemm¹, Shirin Mozaffari², Rui Zhang¹, Brian W. Casas², Alexei E. Koshelev³, Ming Yi¹, Luis Balicas^{2,*}, and Pengcheng Dai^{1,**}

1. Department of Physics and Astronomy, Rice University, Houston, TX 77005 USA
2. National High Magnetic Field Laboratory, Florida State University, Tallahassee, FL 32310 USA
3. Materials Science Division, Argonne National Laboratory, Lemont, IL 60439 USA

We use transport measurements to determine the in-plane anisotropy of the upper critical field H_{c2} in detwinned superconducting $\text{Ba}(\text{Fe}_{1-x}\text{M}_x)_2\text{As}_2$ ($\text{M} = \text{Co}, \text{Ni}$) single crystals. In previous measurements on twinned single crystals, the charge carrier doping dependence (x) of the upper critical field anisotropy for fields along the inter-planar (c -axis) and in-plane field directions was found to increase in the overdoped regime. For underdoped samples, which exhibit a spin nematic phase below the tetragonal to orthorhombic structural transition temperature T_s , we find that H_{c2} along the a -axis is considerably lower than that along the b -axis. The upper critical field anisotropy disappears in the over-doped regime when the system becomes tetragonal. By combining these results with inelastic neutron scattering studies of spin excitations, and angle-resolved photoemission spectroscopy, we conclude that superconductivity in under-doped iron pnictides is orbital selective – with a dominant contribution from electrons with the d_{yz} orbital character and being intimately associated with spin excitations.

In conventional Bardeen–Cooper–Schrieffer (BCS) superconductors, electrons form coherent Cooper pairs below the superconducting transition temperature through interacting with the lattice ¹. If the electrons forming Cooper pairs mostly originate from a single electronic band, the superconducting state is the ground state and does not coexist with charge- or spin- density wave order originating from the superconducting electronic band ². However, there are many multiband BCS superconductors, such as MgB₂ ^{3,4} and NbSe₂ ^{5,6}, where superconductivity can occur in a specific band with an orbital selective superconducting gap. While unconventional copper oxide superconductors are single band materials ⁷⁻⁹, iron-based superconductors are known multiband materials where superconductivity may occur through an orbital-selective pairing mechanism analogous to that of multiband BCS superconductors ¹⁰⁻¹³. Most unconventional superconductors, in contrast to BCS superconductors, have nonsuperconducting antiferromagnetic (AF) ordered parents and superconductivity arises from electron/hole doping that suppresses the AF order ^{7-9,14,15}. In the case of iron pnictide superconductors, there is an additional tetragonal-to-orthorhombic structural phase transition at T_s , occurring at or above the collinear static AF ordering temperature T_N ¹⁶. The structural transition is associated with an electronic nematic phase, where transport and electronic properties exhibit twofold rotational symmetry within the nearly square FeAs lattice ¹⁷⁻²¹, and orbital dependent Fermi surface nesting ²²⁻²⁸. With increasing electron doping, T_s and T_N decrease and superconductivity appears as shown schematically in Fig. 1(a) for the Ba(Fe_{1-x}M_x)₂As₂ (M = Co, Ni) families of iron pnictide superconductors ²⁹⁻³³. Given the close connection between magnetism and superconductivity, pairing in these superconducting materials is believed to be mediated by AF spin fluctuations ^{14,15}, arising from quasiparticle excitations between the sign reversed hole and electron Fermi surfaces at different parts of the Brillouin zone

³⁴. This manifests experimentally as a resonance, or a collective magnetic excitation at an energy E_r appearing below the superconducting transition temperature T_c with its intensity tracking the superconducting order parameter, in the spin excitation spectra ^{14,15,35-37}. In the weak-coupling theory of superconductivity, the resonance is a bound state arising from quasiparticle excitations that connect parts of the Fermi surfaces exhibiting a sign change in the superconducting order parameter $\Delta(\mathbf{k}) = -\Delta(\mathbf{k} + \mathbf{Q})$, where $\Delta(\mathbf{k})$ is the momentum (\mathbf{k})-dependent superconducting gap and \mathbf{Q} is the momentum transfer connecting the two gapped Fermi surfaces ^{14,15,35-37}.

The left inset in Figure 1(a) shows the collinear static AF structure of BaFe_2As_2 , the parent compound of $\text{Ba}(\text{Fe}_{1-x}\text{M}_x)_2\text{As}_2$ families of iron pnictide superconductors ¹⁵. In the underdoped regime, these materials exhibit a tetragonal-to-orthorhombic structural transition at T_s , a collinear static AF order below T_N , and superconductivity below T_c [$T_s > T_N > T_c$]. When the doping reaches the optimal level for superconductivity [$x = 0.06$ (M=Co) and 0.04 (M=Ni)] and beyond, the system becomes tetragonal at all temperatures. With further doping increase, superconductivity vanishes for doping levels above $x = 0.13$ (M=Co) [Fig. 1(a)] ²⁹⁻³³. For the iron pnictides, angle resolved photoemission spectroscopy experiments reveal that three Fe t_{2g} orbitals (d_{xz} , d_{yz} , d_{xy}) are active near the Fermi level forming hole and electron Fermi pockets as shown in Fig. 1(b) ^{13,38}. Nesting among electron-hole Fermi surface sheets associated with quasiparticles on the d_{xz} and d_{yz} orbitals occurs along the \mathbf{Q}_1 and \mathbf{Q}_2 directions, respectively, and can induce spin excitations along these two directions ³⁹. In the paramagnetic tetragonal state, the degenerate d_{xz} and d_{yz} orbitals induce these spin excitations with equal intensity at \mathbf{Q}_1 and \mathbf{Q}_2 . In the underdoped regime upon cooling below T_s the d_{yz} band of the electron Fermi surface at X/Y increases in energy, while the d_{xz} band decreases in energy ^{40,41}. Better nesting conditions

resulting from the shifting of the bands lead to orbital selective spin excitations for d_{yz} orbitals along the Q_I direction^{42,43}. If the neutron spin resonance is associated with the superconducting electron pairing, these results would suggest that superconductivity in iron arsenides and selenides is orbital selective^{11,12,42,44,45} and dominated by the d_{yz} orbitals with associated AF fluctuations along the Q_I direction. For underdoped $\text{Ba}(\text{Fe}_{1-x}\text{M}_x)_2\text{As}_2$ where superconductivity co-exists microscopically with static AF order¹⁵, there is a reduction of static ordered magnetic moment below T_c due to its competition with superconductivity^{29,46,47}. Therefore, one would expect an anisotropic superconducting state within the orthorhombic lattice plane of the underdoped regime that disappears when the crystal becomes tetragonal in the overdoped regime without AF order at all temperatures. Here, using transport measurements, we report that the anisotropy of the in-plane upper critical fields H_{c2} of underdoped $\text{Ba}(\text{Fe}_{1-x}\text{M}_x)_2\text{As}_2$ is consistent with an orbital selective pairing that involves electrons having d_{yz} orbital character.

The presence of twin domains in large single crystals of underdoped $\text{Ba}(\text{Fe}_{1-x}\text{M}_x)_2\text{As}_2$ renders conventional measurements insufficient to distinguish the rotational symmetry breaking between the d_{xz} and d_{yz} orbitals that occurs below T_s , meaning that neither orbital can be unambiguously determined to be associated with superconductivity in such a state. Therefore, uniaxial pressure must be used to obtain a single domain from which the intrinsic magnetic and electronic properties can be determined⁴⁸. Electronic nematicity below T_s has long been established in the $\text{Ba}(\text{Fe}_{1-x}\text{M}_x)_2\text{As}_2$ materials through the process of detwinning¹⁷⁻²¹. The schematic provided in the left inset of Fig. 1(a) details the in-plane AF ordering with respect to the direction of the applied uniaxial pressure. Recent neutron scattering experiments on detwinned, underdoped $\text{Ba}(\text{Fe}_{1-x}\text{Co}_x)_2\text{As}_2$ reveal anisotropic spin fluctuations, with the neutron spin resonance associated with superconductivity observed along the AF wavevector, $Q_I = (1,0)$,

and no magnetic scattering observed along $Q_2 = (0,1)$ ⁴². Additionally, the Fermi surface is modified below T_s in underdoped single crystals and, consequently, of the nesting condition [Figs. 1(b-c)]^{13,40}. Although the upper critical field anisotropy for in-plane and c -axis aligned magnetic fields has been heavily investigated for different families of iron-based superconductors^{33,49-56}, there is no report of in-plane upper critical field anisotropy for $\text{Ba}(\text{Fe}_{1-x}\text{M}_x)_2\text{As}_2$ having the orthorhombic lattice structure in the underdoped regime.

Single-crystals were grown with $\text{Fe}_{1-x}\text{M}_x\text{As}$ as the chosen flux via the self-flux method⁵⁷. We chose to study underdoped $\text{Ba}(\text{Fe}_{1-x}\text{Ni}_x)_2\text{As}_2$ with $x \sim 0.04$, which has a $T_N \sim 44$ K where AF order coexists with superconductivity below $T_c \sim 17$ K^{47,58}, and overdoped $\text{Ba}(\text{Fe}_{1-x}\text{Co}_x)_2\text{As}_2$ with $x = 0.11$ ³⁰. Larger single crystals were aligned and later cut along the orthorhombic a and b axes into roughly 2x2 mm squares using a Laue x-ray diffractometer and a wire saw respectively. Samples were then detwinned via uniaxial pressure with a small brass clamp. To investigate a potential orbital selective pairing mechanism, we probe the anisotropy of the in-plane upper critical fields of underdoped $\text{Ba}(\text{Fe}_{1-x}\text{Ni}_x)_2\text{As}_2$ via resistivity measurements along the c axis by using a Corbino geometry and an in-plane DC field [Fig. 1(d)]⁵⁰. We use a Corbino-like geometry for the electrical contacts to maximize the cross-sectional area of the sample within the ab -plane, and to ensure a higher homogeneity for the electrical current density flowing along the c -axis. High current homogeneity and large cross-sectional areas are not achievable with other configurations for the electrical contacts. Field dependent measurements of T_c were first conducted using the rotator option of a Quantum Design Physical Properties Measurement System with the later measurements performed at the National High Magnetic Field Laboratory using both a superconducting 18 T magnet and a 41 T resistive Bitter magnet, respectively. Our results reveal a clear anisotropy in the upper critical fields of underdoped $\text{Ba}(\text{Fe}_{1-x}\text{Ni}_x)_2\text{As}_2$, with

the field along the a -axis resulting in a lower projected H_{c2} relative to fields aligned along the b axis (Figs. 2-4).

To systematically characterize T_c , a range of magnetic fields were applied along the a and b axes of each sample and then temperature was swept across the superconducting transition while maintaining a constant applied field. A schematic of the geometric relationship between the applied field direction, crystal axes, and strain direction is indicated in Fig. 1(d). It is clear from the raw resistivity data that a planar anisotropy exists in the underdoped samples [Fig. 2(a,c,e)]. Traces of identical colors correspond to the same magnitude of the applied magnetic field with the lighter and darker shade of the same color representing the direction of the field, i.e., along the a and b axes, respectively. From these temperature sweeps, we extract the onset of T_c which we define as 90% of the value of the resistivity in the normal state just above T_c . A sample-dependent, anomalous hump appears before the onset of superconductivity in some of our measurements. Strain free measurements reveal the hump only appears after pressure is applied to the sample (see supplementary Fig. S1). In these cases, we treat the 90% criterion as 90% of the normal state resistivity before the upturn of the humps [Fig. 2(a)]. Note that the apparent anisotropy depends on the definition of the onset as reflected in a similar work⁵³. Since the evaluation of the superconducting gap function would require an array of thermodynamic, spectroscopic, and transport techniques, transport measurements alone cannot conclusively determine the absolute magnitude of the superconducting gap anisotropy. Nevertheless, from the transport measurements we can evaluate the anisotropy of the characteristic energy scale required for thermally activated flux flow of vortices (see Supplemental Fig. S5).

One important question to address is the impact of magnetic order and associated magnetoresistance to the observed H_{c2} anisotropy relative to fields aligned along the a and b

axis. From in-plane magnetic field neutron diffraction measurements on twinned $\text{Ba}(\text{Fe}_{1-x}\text{Ni}_x)_2\text{As}_2$ with $x \sim 0.04$ ($T_c = 17$ K and $T_N \approx 44$ K), an identical doping level as our current transport measurements, an in-plane magnetic field of 10-T has no observable impact on magnetic ordered moment, T_N , or spin fluctuations in the normal state (above T_c) but can recover superconductivity-suppressed static magnetic ordered moment below T_c ⁴⁷. Since the magnetoresistance in the normal (nonsuperconducting) state of $\text{Ba}(\text{Fe}_{1-x}\text{Ni}_x)_2\text{As}_2$ with $x = 0.04$ ($T \sim 18$ K) is at most 0.01% for a 20-T in-plane field and has no observable anisotropy for fields aligned along the a and b direction (Supplementary Figs. S6-7), we conclude that the observed H_{c2} anisotropy for fields aligned along the a and b in Fig. 2 is due to the suppression of superconductivity and unrelated to the static AF order.

Because the electronic nematic phase is believed to be associated with the unidirectional spin resonance observed by inelastic neutron scattering, and thus the orbital selective pairing, we can explore the overdoped side of the phase-diagram to further test this hypothesis^{17,30,42,52}. Overdoped single crystals experience no structural phase transitions associated with electronic nematicity but do retain a superconducting transition at a comparable T_c [Fig. 1(a)]. Identical resistivity measurements with uniaxial strain on overdoped samples reveal no anisotropy in the upper critical fields like the one seen for the underdoped single crystals [Fig. 2(b,d,f)]. Therefore, the anisotropy of H_{c2} observed in the underdoped sample and the lack of thereof in the overdoped sample indicate that the observed anisotropic H_{c2} in the former is not due to applied uniaxial pressure, but to the orbital selective nature of the pairing contingent upon the existence of an electronic nematic phase.

The Montgomery method was utilized to capture the planar resistivity when the magnetic field is applied along either the a or b axes as pictured in the inset of Figs. 3(b,d)^{59,60}. The

purpose of these measurements is to test the differences in resistivity for current along and perpendicular to the applied magnetic field direction. Figures 3(a) and 3(c) summarize the results for underdoped single crystals with current along the a -axis and b -axis, respectively. While fields along the b -axis suppress T_c more significantly than fields along the a -axis according to inter-planar resistivity measurements, the suppression of T_c as probed via the planar resistivity depends on the relative orientation between the field and the electrical currents. Specifically, T_c experiences a more dramatic suppression near the transition temperature when the applied field and the electric current are perpendicular to one another. A sample on the overdoped side with a slightly higher T_c , measured via this configuration, still reveals a very small anisotropy [Figs. 3(b-d)]. The higher T_c of the overdoped samples is consistent with a closer proximity to the nematic phase, which vanishes near optimal superconductivity, compared with overdoped samples with the same T_c as that of the underdoped one [Fig. 1(a)]. In this configuration, one cannot exclude the possibility that this anisotropy might result from the relative alignment between the electrical currents and the external field or their interactions. Nevertheless, temperature sweeps for various applied currents reveal negligible differences in T_c , ruling out the magnitude of the current as being responsible for the observed anisotropy (see Supplementary Fig. S2). Therefore, the c -axis resistivity is the most appropriate configuration to characterize this anisotropy because the relationship between the externally applied field and the electrical current is maintained constant, in other words they are always kept perpendicular to each other. In particular, there are clear differences in zero resistance temperatures for field applied along the a -axis and b -axis in the underdoped sample for fields above 20-T, when T_c is suppressed to below 10 K [Fig. 2(e)]. Since we do not have data above 20-T in the Montgomery

method discussed in Fig. 3, it is difficult to reach a conclusion about in-plane upper critical field anisotropy using these results.

Further analysis on the raw data in Fig. 2 was performed to extract the evolution of the onset T_c as a function of the increasing field for both underdoped and overdoped samples [Figs. 4(a-b)]. Clearly, the anisotropy in H_{c2} exists exclusively in the underdoped sample in this representation. The conditionality of the planar H_{c2} in the underdoped samples becomes more evident by plotting the T_c onset, demonstrating a faster suppression of the transport T_c near the zero-field transition temperature when the field and the electrical current are perpendicular [Figs. 4(c-d)]. Plotting ρ_a and ρ_b when the field and current are parallel reveals minor anisotropy that increases at higher field [Fig. 4(e)]. The case where the field and electrical current are perpendicular result in no anisotropy within error bars [Fig. 4(f)].

In general, the anisotropy of the upper critical field may be caused by either anisotropy of Fermi velocity or gap and the first factor is more common. For the case of underdoped $\text{Ba}(\text{Fe}_{1-x}\text{Ni}_x)_2\text{As}_2$ materials with nematic order, several factors may contribute to the anisotropy of H_{c2} : (i) the hole bands become anisotropic, (ii) anisotropies and occupations of the two electron bands become different, and (iii) the interband pairings between the hole bands and two electron bands become different leading to different superconducting gaps in the two electron bands. We believe that the last mechanism likely dominates due to strong modification of the nesting conditions upon entering the nematic state. Upon cooling from the normal state, the d_{yz} band along the Γ -X direction is lifted towards the Fermi energy (E_F) while the d_{xz} band along Γ -Y drops in energy relative to E_F , thus breaking the degeneracy between the two bands¹³. This should favor nesting between the Fermi surface sheets associated with the d_{yz} bands when compared to those of the d_{xz} bands as illustrated in Figs. 1(b-c). Such a nesting condition would provide a clear explanation

for the observed magnetic scattering along Q_1 and Q_2 in recent work^{42,43}. If superconducting electron pairing in the iron pnictides is driven by spin fluctuations, as is widely suspected, we should expect pairing to occur as the result of d_{yz} - d_{yz} intra-orbital fluctuations, *i.e.*, an orbital selective pairing mechanism. A dramatic consequence of such a pairing mechanism would mean that the superconducting gaps are different for electrons with d_{yz} and d_{xz} orbital characters along the (1,0) and (0,1) directions, respectively. Therefore, we would also expect the upper critical fields of this system, at which the superconducting pairing breaks down, to be directionally dependent between the (1,0) and (0,1) directions in the underdoped regime. Our results in Fig. 4 reflect this anisotropy. It follows, then, that the overdoped single crystals should see no evidence of anisotropy among in-plane upper critical fields, as these samples experience no transition into a nematic state and therefore no modification of the nesting condition in the band structure. Indeed, there is no upper critical field anisotropy for overdoped samples under a similar uniaxial strain [Fig. 4(b)]. Therefore, our systematic upper critical field measurements support the notion that superconductivity in the underdoped iron pnictide superconductors is orbital selective, or clearly different from an isotropic s -wave superconductors. These results are consistent with twofold oscillations of angular dependence of the in-plane and out-of-plane magnetoresistivity of $\text{Ba}_{0.5}\text{K}_{0.5}\text{Fe}_2\text{As}_2$ near T_c when the direction of the applied field is rotated within the plane⁶¹. We note that similar anisotropic upper critical fields have been reported for twisted bilayer graphene, as a sign of nematic superconducting pairing⁶². In that case, orbital-selective superconductivity is also the proposed mechanism, involving multi-component pairing⁶³.

We note that several Fe based superconductors display upper critical fields exceeding the Pauli limiting field⁴⁹. The reason for this remains controversial, although it was often ascribed to the multi-band nature of the superconductivity in these compounds. One possibility, particularly

for more disordered chemically doped samples, is that this renormalization results from spin orbit scattering, usually treated in terms of an isotropic spin-orbit scattering time τ_{so} ⁶⁴. Alternatively, anisotropy of the potential scattering time may also contribute to the observed anisotropy.

It is well known that the scattering rate in the $\text{Ba}(\text{Fe}_{1-x}\text{M}_x)_2\text{As}_2$ family of Fe based pnictide superconductors is rather anisotropic^{20,65,66}. The reason for this anisotropy is not well understood, but it might reflect the intrinsic nematicity of the underlying electronic fluid from which superconductivity condenses⁶⁷. In this scenario, one would expect that τ_{so} becomes anisotropic in the underdoped $\text{Ba}(\text{Fe}_{1-x}\text{M}_x)_2\text{As}_2$ compounds below T_N but above T_c , leading to the anisotropy in upper critical fields observed here. However, we find a very small resistivity anisotropy associated with the electronic nematicity in the underdoped region of these compounds (See supplementary Fig. S6).

In summary, we use a series of resistivity measurements to analyze the anisotropy of the in-plane H_{c2} s for uniaxial strain detwinned crystals of the iron pnictide superconductor $\text{Ba}(\text{Fe}_{1-x}\text{M}_x)_2\text{As}_2$. For underdoped samples with an orthorhombic lattice structure, we find a clear in-plane upper critical field anisotropy in uniaxial strain detwinned samples for fields above 20-T with a c -axis current. These results are consistent with an orbital selective electron pairing, where the superconducting gap along the (1,0) direction with d_{yz} orbital character is larger than that along the (0,1) direction with d_{xz} orbital character. Therefore, superconductivity in the underdoped regime acquires a “nematic” character when it condenses from this electronic/spin state⁶⁷. For the overdoped samples with a tetragonal lattice structure and without a nematic phase, similar measurements show no evidence of anisotropy in the in-plane upper critical fields. These results are consistent with an orbital selective pairing mechanism, suggesting that the quasiparticle excitations between electron-hole Fermi surface pockets having a d_{yz} orbital

character are favorable for electron pairing. These results further confirm that superconductivity is likely mediated by spin fluctuations associated with the electron-hole quasiparticle excitations in iron based superconductors ¹⁴.

The experimental and basic materials synthesis work at Rice is supported by the U.S. DOE, BES under Grant No. DE-SC0012311 and by the Robert A. Welch Foundation under Grant No. C-1839, respectively (P.D.). L.B. is supported by the US DOE, Basic Energy Sciences program through award DE-SC0002613. M.Y. acknowledges support by the Gordon and Betty Moore Foundation's EPiQS Initiative through grant no. GBMF9470, and the Robert A. Welch Foundation, Grant No. C-2175. The National High Magnetic Field Laboratory acknowledges support from the US-NSF Cooperative agreement Grant number DMR-1644779 and the state of Florida. Work of A.E.K at Argonne National Laboratory was funded by the US Department of Energy, Office of Science, Basic Energy Sciences, Materials Sciences and Engineering Division.

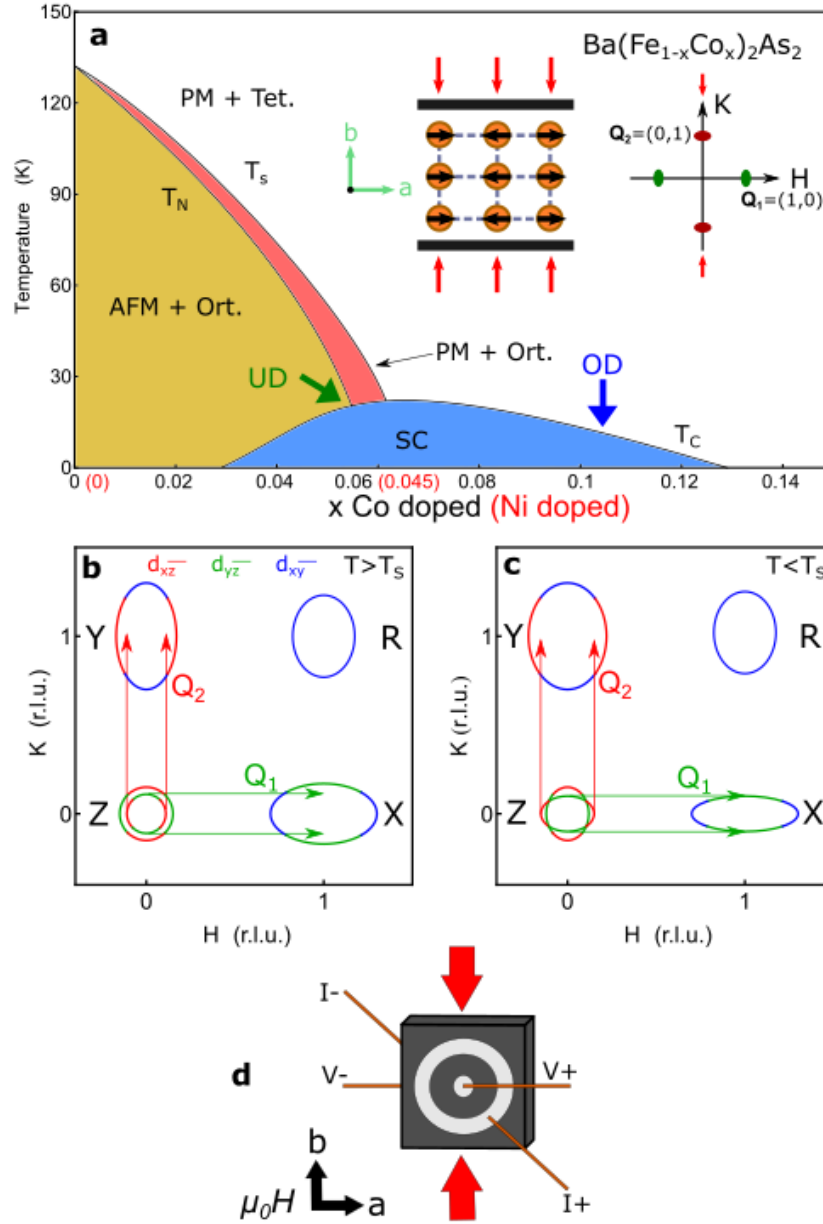


Fig. 1 (a) Phase diagram denoting the rough doping of the underdoped (UD) and overdoped (OD) samples. Note that the horizontal axis is modified for Ni doped samples, as Ni contributes approximately twice as many electrons as Co. The first inset describes the orientation of the strain (red arrows) relative to the antiferromagnetic ordering defining the a and b axes. The second inset reflects the AF wavevector \mathbf{Q}_1 (green) and wavevector \mathbf{Q}_2 (red) studied in prior neutron scattering work [29-32]. (b) Illustrative Fermi surfaces and associated orbital contributions for the paramagnetic tetragonal lattice and the (c) nematic state below T_s for the simplified two-dimensional unfolded Brillouin zone. The arrows show the nesting wavevectors \mathbf{Q}_1 and \mathbf{Q}_2 . (d) Corbino geometry used to measure resistivity along the c -axis. The back surface of the crystal is identically wired to that which is illustrated for the front surface.

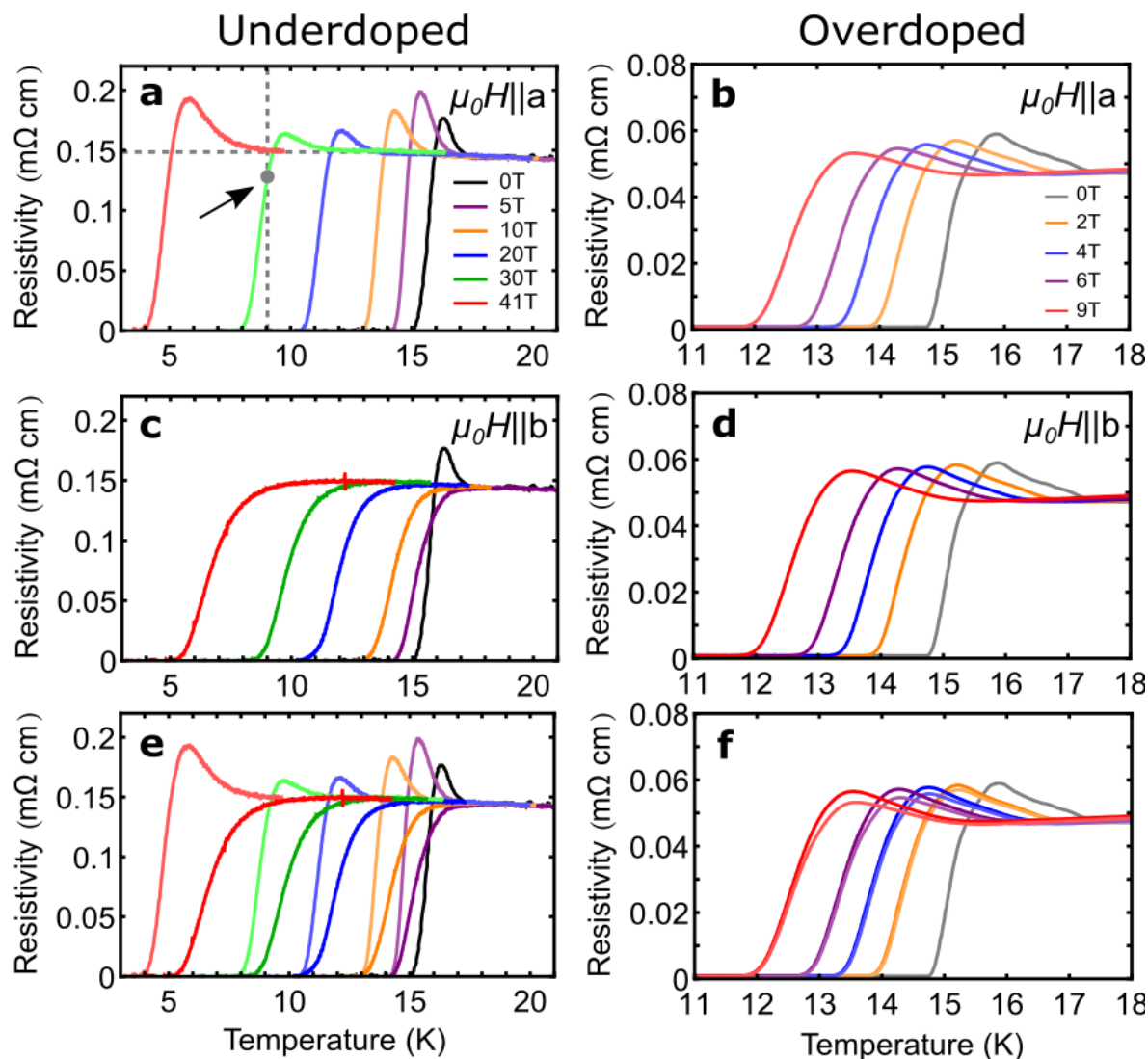


Fig. 2 Resistivity measured using a Corbino geometry (ρ_{zz}) as a function of the temperature under varying field strengths applied along the a -axis for underdoped (a) and overdoped (b) samples. Data for field along the b -axis for underdoped and overdoped samples are given in (c) and (d) respectively. (e) Same data as in panels (a) and (c) but plotted together to illustrate the anisotropy in upper critical fields inherent to the underdoped sample. Similarly, (b) and (d) are combined in (f) to illustrate the contrasting lack of anisotropy. Treatment of the 90% criterion in the presence of the humps is illustrated in panel (a) with the arrow noting the point on the curve at which the resistivity drops to 90% of its normal state value. Notice that the peaks preceding the superconducting transition are not observed in the absence of strain, with their presence along a specific field crystallographic orientation requiring further theoretical understanding. Notice also, that at the highest magnetic fields the zero-resistance state (vortex solid phase) is achieved at higher temperatures for both crystallographic orientations, implying that the observed anisotropy is unrelated to the flux flow of vortices. The normal state resistivity of the 41T data in the underdoped sample was normalized to the normal state resistivity of the other curves.

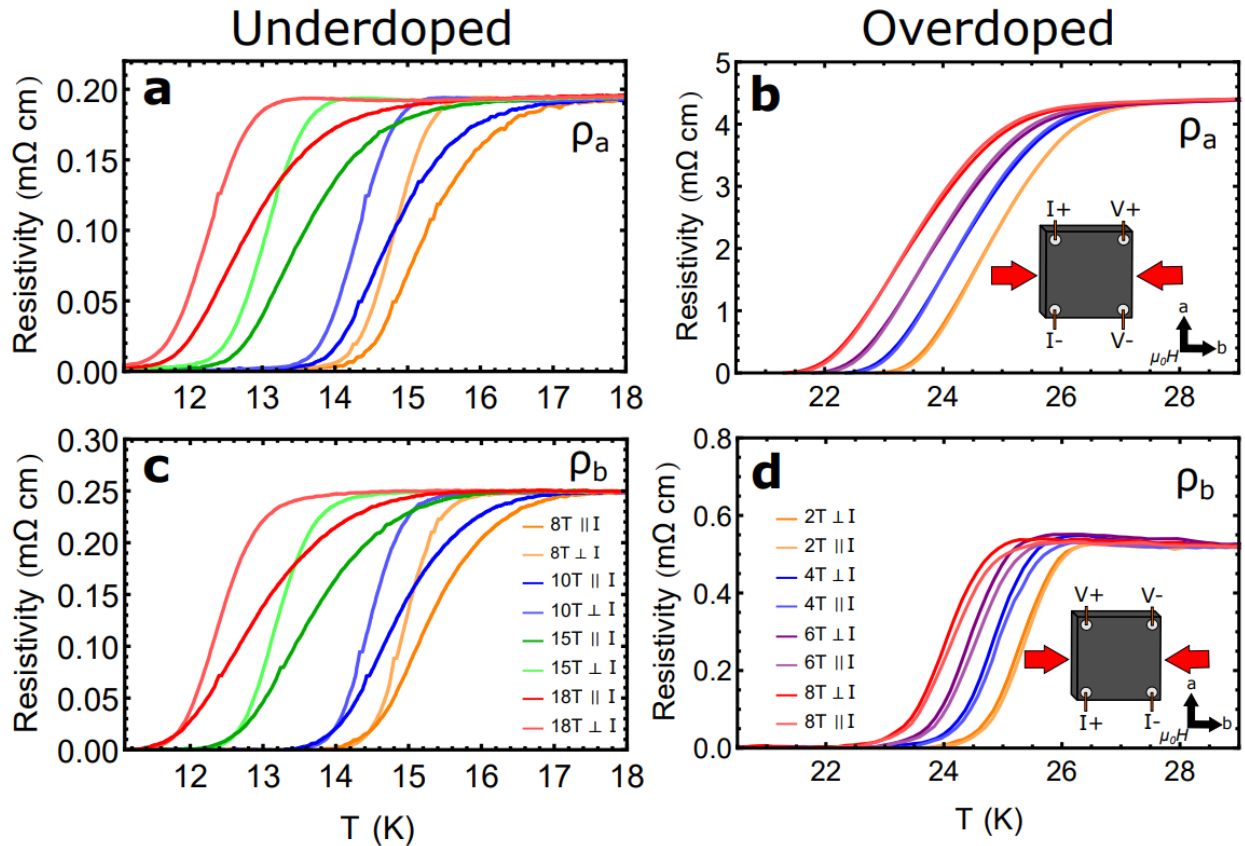


Fig. 3 (a) and (b) Resistive transitions as a function of T revealing the values of the upper critical fields μ_0H_{c2} for strain applied along the b -axis and current along the a -axis and for both planar field orientations for underdoped and overdoped samples, respectively. Data for the currents along the b -axis is similarly presented for underdoped and overdoped samples in (c) and (d) respectively. Insets in (b) and (d) are schematics depicting the directions of the current (I+/-), strain (red arrows), and magnetic fields along crystalline axes a and b for each measurement. Regardless of the current orientation relative to strain, one always observes a larger inset field for currents aligned along the planar field.

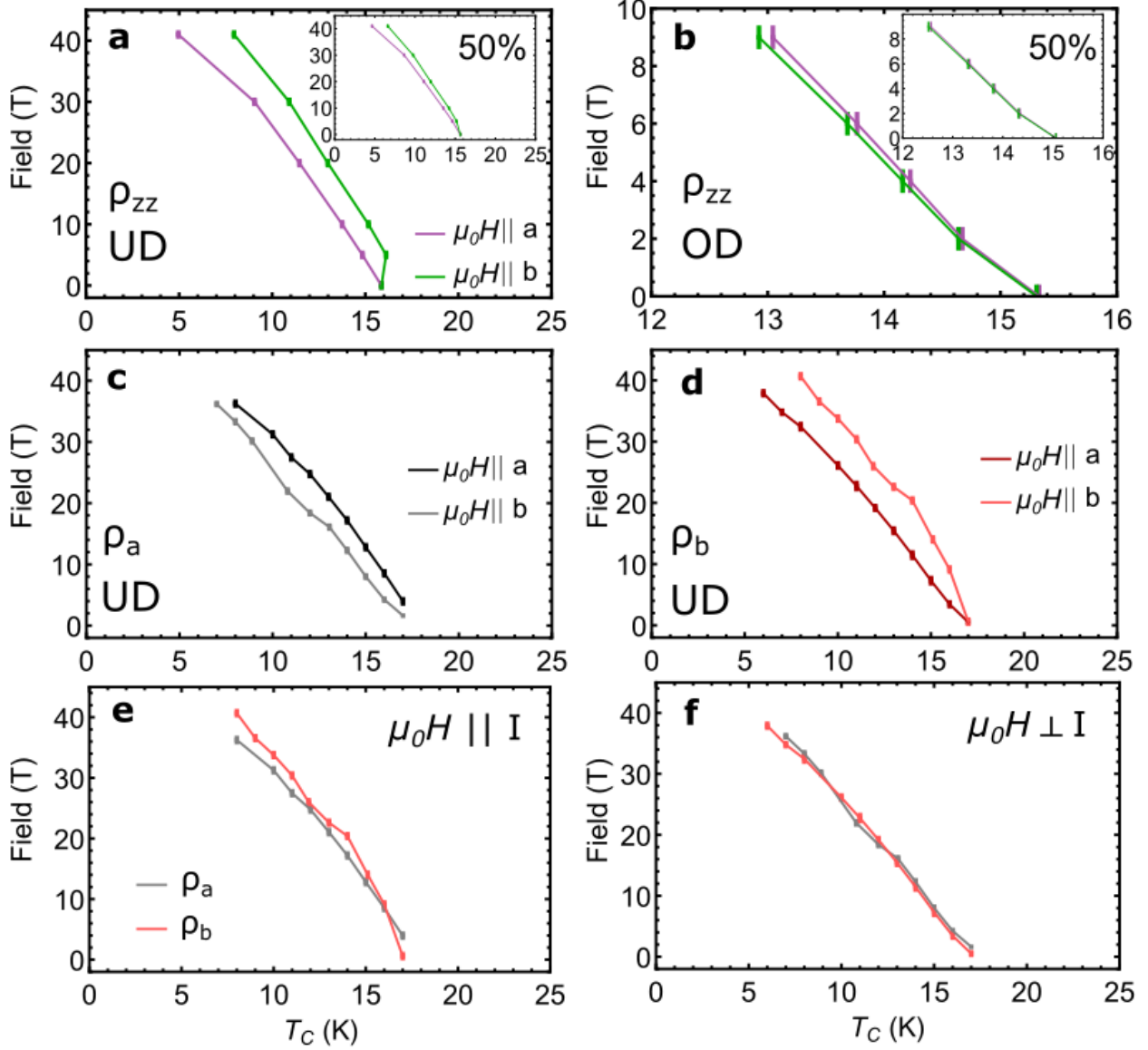


Fig. 4 (a) H_{c2} as a function of the temperature (T) when measured through the interplanar resistivity ρ_{zz} for an underdoped sample using the 90% criterion. (b) $H_{c2}(T)$ for an overdoped sample as extracted from ρ_{zz} . The insets for (a) and (b) display the extracted $H_{c2}(T)$ using the 50% criterion. (c) and (d) H_{c2} for an underdoped sample as a function of T and as extracted from the in-plane resistivities, ρ_a and ρ_b , respectively. (e) and (f) In-plane resistivity from (c) and (d) plotted such that the field and current are parallel and perpendicular respectively. Error bars are assigned to the extracted H_{c2} to account for the humps. During the 90% criterion analysis, the normal state resistivity was considered from the peak of the hump to the flat region above the superconducting transition. The range of H_{c2} resulting from the different definitions of the normal state resistivity is what determines the size of the error bars. This is a liberal estimation of the measurement error. Notice that the anisotropy in upper critical fields increases continuously as the temperature is lowered, in contrast to the anisotropy extracted for the activation energy for vortex flux flow (see Fig. S5). Therefore, the anisotropy in upper critical fields extracted using the 90% of the resistive transition criteria ought to be intrinsic, or is unrelated to vortex physics.

*email: balicas@magnet.fsu.edu

**email: pdai@rice.edu

- 1 Bardeen, J., Cooper, L. & Schrieffer, J. Microscopic Theory of Superconductivity. *Physical Review* **106**, 162-164, doi:10.1103/PhysRev.106.162 (1957).
- 2 Sipos, B. *et al.* From Mott state to superconductivity in 1T-TaS₂. *Nature Materials* **7**, 960-965, doi:10.1038/nmat2318 (2008).
- 3 Nagamatsu, J., Nakagawa, N., Muranaka, T., Zenitani, Y. & Akimitsu, J. Superconductivity at 39 K in magnesium diboride. *Nature* **410**, 63-64 (2001).
- 4 Li, Q. *et al.* Large Anisotropic Normal-State Magnetoresistance in Clean MgB₂ Thin Films. *Physical Review Letters* **96**, 167003, doi:10.1103/PhysRevLett.96.167003 (2006).
- 5 Yokoya, T. *et al.* Fermi Surface Sheet-Dependent Superconductivity in 2H-NbSe₂. *Science* **294**, 2518-2520, doi:10.1126/science.1065068 (2001).
- 6 Heil, C. *et al.* Origin of Superconductivity and Latent Charge Density Wave in NbS_2 . *Physical Review Letters* **119**, 087003, doi:10.1103/PhysRevLett.119.087003 (2017).
- 7 Lee, P. A., Nagaosa, N. & Wen, X.-G. Doping a Mott insulator: Physics of high-temperature superconductivity. *Reviews of Modern Physics* **78**, 17-85 (2006).
- 8 Stewart, G. R. Unconventional superconductivity. *Advances in Physics* **66**, 75-196, doi:10.1080/00018732.2017.1331615 (2017).
- 9 Keimer, B., Kivelson, S. A., Norman, M. R., Uchida, S. & Zaanen, J. From quantum matter to high-temperature superconductivity in copper oxides. *Nature* **518**, 179-186, doi:10.1038/nature14165 (2015).
- 10 Fernandes, R. M. *et al.* Iron pnictides and chalcogenides: a new paradigm for superconductivity. *Nature* **601**, 35-44, doi:10.1038/s41586-021-04073-2 (2022).
- 11 Sprau, P. O. *et al.* Discovery of orbital-selective Cooper pairing in FeSe. *Science* **357**, 75, doi:10.1126/science.aal1575 (2017).
- 12 Nica, E. M., Yu, R. & Si, Q. Orbital-selective pairing and superconductivity in iron selenides. *npj Quantum Mater.* **2**, 24, doi:10.1038/s41535-017-0027-6 (2017).
- 13 Yi, M., Zhang, Y., Shen, Z.-X. & Lu, D. Role of the orbital degree of freedom in iron-based superconductors. *npj Quantum Mater.* **2**, 57, doi:10.1038/s41535-017-0059-y (2017).
- 14 Scalapino, D. J. A common thread: The pairing interaction for unconventional superconductors. *Reviews of Modern Physics* **84**, 1383-1417 (2012).
- 15 Dai, P. Antiferromagnetic order and spin dynamics in iron-based superconductors. *Reviews of Modern Physics* **87**, 855-896, doi:10.1103/RevModPhys.87.855 (2015).
- 16 de la Cruz, C. *et al.* Magnetic order close to superconductivity in the iron-based layered LaO_{1-x}F_xFeAs systems. *Nature* **453**, 899, doi:10.1038/nature07057 <https://www.nature.com/articles/nature07057#supplementary-information> (2008).
- 17 Chu, J.-H. *et al.* In-Plane Resistivity Anisotropy in an Underdoped Iron Arsenide Superconductor. *Science* **329**, 824-826, doi:10.1126/science.1190482 (2010).
- 18 Tanatar, M. A. *et al.* Uniaxial-strain mechanical detwinning of CaFe₂As₂ and BaFe₂As₂ crystals: Optical and transport study. *Physical Review B* **81**, 184508 (2010).
- 19 Chuang, T.-M. *et al.* Nematic Electronic Structure in the “Parent” State of the Iron-Based Superconductor Ca(Fe_{1-x}Cox)₂As₂. *Science* **327**, 181-184, doi:10.1126/science.1181083 (2010).
- 20 Allan, M. P. *et al.* Anisotropic impurity states, quasiparticle scattering and nematic transport in underdoped Ca(Fe_{1-x}Cox)₂As₂. *Nat Phys* **9**, 220-224, doi:<http://www.nature.com/nphys/journal/v9/n4/abs/nphys2544.html#supplementary-information> (2013).

- 21 Böhmer, A. E., Chu, J.-H., Lederer, S. & Yi, M. Nematicity and nematic fluctuations in iron-based superconductors. *Nature Physics* **18**, 1412-1419, doi:10.1038/s41567-022-01833-3 (2022).
- 22 Kim, Y. *et al.* Electronic structure of detwinned BaFe₂As₂ from photoemission and first principles. *Physical Review B* **83**, 064509, doi:10.1103/PhysRevB.83.064509 (2011).
- 23 Zhang, Y. *et al.* Symmetry breaking via orbital-dependent reconstruction of electronic structure in detwinned NaFeAs. *Physical Review B* **85**, 085121 (2012).
- 24 Ge, Q. Q. *et al.* Anisotropic but Nodeless Superconducting Gap in the Presence of Spin-Density Wave in Iron-Pnictide Superconductor NaFe_{1-x}CoxAs. *Physical Review X* **3**, doi:10.1103/PhysRevX.3.011020 (2013).
- 25 Suzuki, Y. *et al.* Momentum-dependent sign inversion of orbital order in superconducting FeSe. *Physical Review B* **92**, 205117, doi:10.1103/PhysRevB.92.205117 (2015).
- 26 Pfau, H. *et al.* Momentum Dependence of the Nematic Order Parameter in Iron-Based Superconductors. *Physical Review Letters* **123**, 066402, doi:10.1103/PhysRevLett.123.066402 (2019).
- 27 Watson, M. D. *et al.* Evidence for unidirectional nematic bond ordering in FeSe. *Physical Review B* **94**, 201107, doi:10.1103/PhysRevB.94.201107 (2016).
- 28 Yi, M. *et al.* Nematic Energy Scale and the Missing Electron Pocket in FeSe. *Physical Review X* **9**, 041049, doi:10.1103/PhysRevX.9.041049 (2019).
- 29 Pratt, D. K. *et al.* Coexistence of Competing Antiferromagnetic and Superconducting Phases in the Underdoped Ba(Fe_{0.953}Co_{0.047})₂As₂ Compound Using X-ray and Neutron Scattering Techniques. *Physical Review Letters* **103**, 087001 (2009).
- 30 Nandi, S. *et al.* Anomalous Suppression of the Orthorhombic Lattice Distortion in Superconducting Ba(Fe_{1-x}Cox)₂As₂ Single Crystals. *Physical Review Letters* **104**, 057006 (2010).
- 31 Luo, H. Q. *et al.* Electron doping evolution of the anisotropic spin excitations in BaFe_{2-x}NixAs₂. *Physical Review B* **86**, doi:10.1103/PhysRevB.86.024508 (2012).
- 32 Lu, X. Y. *et al.* Avoided Quantum Criticality and Magnetoelastic Coupling in BaFe_{2-x}NixAs₂. *Physical Review Letters* **110**, 257001, doi:ARTN 257001 10.1103/PhysRevLett.110.257001 (2013).
- 33 Ni, N. *et al.* Temperature versus doping phase diagrams for Ba_{1-x}TM_xAs₂ (TM = Ni, Cu, Co) single crystals. *Physical Review B* **82**, 024519, doi:10.1103/PhysRevB.82.024519 (2010).
- 34 Hirschfeld, P. J., Korshunov, M. M. & Mazin, I. I. Gap symmetry and structure of Fe-based superconductors. *Reports on Progress in Physics* **74**, 124508 (2011).
- 35 Eschrig, M. The effect of collective spin-1 excitations on electronic spectra in high T_c superconductors. *Advances in Physics* **55**, 47 - 183 (2006).
- 36 Yu, G., Li, Y., Motoyama, E. M. & Greven, M. A universal relationship between magnetic resonance and superconducting gap in unconventional superconductors. *Nat Phys* **5**, 873-875, doi:http://www.nature.com/nphys/journal/v5/n12/supinfo/nphys1426_S1.html (2009).
- 37 Duan, C. *et al.* Resonance from antiferromagnetic spin fluctuations for superconductivity in UTe₂. *Nature* **600**, 636-640, doi:10.1038/s41586-021-04151-5 (2021).
- 38 Yi, M. *et al.* Symmetry-breaking orbital anisotropy observed for detwinned Ba(Fe_{1-x}Cox)₂As₂ above the spin density wave transition. *PNAS* **108**, 6878-6883, doi:10.1073/pnas.1015572108 %J Proceedings of the National Academy of Sciences (2011).

- 39 Dai, P. C., Hu, J. P. & Dagotto, E. Magnetism and its microscopic origin in iron-based high-temperature superconductors. *Nature Physics* **8**, 709-718, doi:10.1038/nphys2438 (2012).
- 40 Pfau, H. *et al.* Detailed band structure of twinned and detwinned BaFe₂As₂ studied with angle-resolved photoemission spectroscopy. *Physical Review B* **99**, 035118, doi:10.1103/PhysRevB.99.035118 (2019).
- 41 Watson, M. D. *et al.* Probing the reconstructed Fermi surface of antiferromagnetic BaFe₂As₂ in one domain. *npj Quantum Mater.* **4**, 36, doi:10.1038/s41535-019-0174-z (2019).
- 42 Tian, L. *et al.* Spin fluctuation anisotropy as a probe of orbital-selective hole-electron quasiparticle excitations in detwinned Ba(Fe_{1-x}Cox)₂As₂. *Physical Review B* **100**, 134509, doi:10.1103/PhysRevB.100.134509 (2019).
- 43 Tam, D. W. *et al.* Orbital selective spin waves in detwinned NaFeAs. *Physical Review B* **102**, 054430, doi:10.1103/PhysRevB.102.054430 (2020).
- 44 Chen, T. *et al.* Anisotropic spin fluctuations in detwinned FeSe. *Nature Materials* **18**, 709, doi:10.1038/s41563-019-0369-5 (2019).
- 45 Kreisel, A., Mukherjee, S., Hirschfeld, P. J. & Andersen, B. M. Spin excitations in a model of FeSe with orbital ordering. *Physical Review B* **92**, 224515, doi:10.1103/PhysRevB.92.224515 (2015).
- 46 Christianson, A. D. *et al.* Static and Dynamic Magnetism in Underdoped Superconductor BaFe_{1.92}Co_{0.08}As₂. *Physical Review Letters* **103**, 087002 (2009).
- 47 Wang, M. *et al.* Magnetic field effect on static antiferromagnetic order and spin excitations in the underdoped iron arsenide superconductor BaFe(1.92)Ni(0.08)As(2). *Physical Review B* **83**, doi:10.1103/PhysRevB.83.094516 (2011).
- 48 Fisher, I. R., Degiorgi, L. & Shen, Z. X. In-plane electronic anisotropy of underdoped '122' Fe-arsenide superconductors revealed by measurements of detwinned single crystals. *Reports on Progress in Physics* **74**, 124506 (2011).
- 49 Yuan, H. Q. *et al.* Nearly isotropic superconductivity in (Ba,K)Fe(2)As(2). *Nature* **457**, 565-568, doi:10.1038/nature07676 (2009).
- 50 Wang, X. F. *et al.* Anisotropy in the Electrical Resistivity and Susceptibility of Superconducting $\text{BaFe}_{1-x}\text{Ni}_x\text{As}_2$ Single Crystals. *Physical Review Letters* **102**, 117005, doi:10.1103/PhysRevLett.102.117005 (2009).
- 51 Her, J. L. *et al.* Anisotropy in the upper critical field of FeSe and FeSe_{0.33}Te_{0.67} single crystals. *Superconductor Science and Technology* **28**, 045013, doi:10.1088/0953-2048/28/4/045013 (2015).
- 52 Wang, Z. *et al.* Electron doping dependence of the anisotropic superconductivity in $\text{BaFe}_{1-x}\text{Ni}_x\text{As}_2$. *Physical Review B* **92**, 174509, doi:10.1103/PhysRevB.92.174509 (2015).
- 53 Llovo, I. F. *et al.* Multiband effects on the upper critical field angular dependence of 122-family iron pnictide superconductors. *Scientific Reports* **11**, 11526, doi:10.1038/s41598-021-90858-4 (2021).
- 54 Welp, U. *et al.* Anisotropic phase diagram and strong coupling effects in Ba(1-x)K(x)Fe(2)As(2) from specific-heat measurements. *Physical Review B* **79**, doi:10.1103/PhysRevB.79.094505 (2009).
- 55 Murphy, J. *et al.* Angular-dependent upper critical field of overdoped Ba(Fe_{1-x}Ni_x)₂As₂. *Physical Review B* **87**, 094505 (2013).
- 56 Gurevich, A. Iron-based superconductors at high magnetic fields. *Reports on Progress in Physics* **74**, 124501, doi:10.1088/0034-4885/74/12/124501 (2011).
- 57 Luo, H. Q. *et al.* Electron doping evolution of the magnetic excitations in BaFe_{2-x}Ni_xAs₂. *Physical Review B* **88**, doi:10.1103/PhysRevB.88.144516 (2013).

- 58 Luo, H. *et al.* Coexistence and Competition of the Short-Range Incommensurate Antiferromagnetic Order with the Superconducting State of $\text{BaFe}_{2-x}\text{Ni}_x\text{As}_2$. *Physical Review Letters* **108**, 247002, doi:10.1103/PhysRevLett.108.247002 (2012).
- 59 Montgomery, H. C. Method for Measuring Electrical Resistivity of Anisotropic Materials. *Journal of Applied Physics* **42**, 2971-2975, doi:doi:<http://dx.doi.org/10.1063/1.1660656> (1971).
- 60 dos Santos, C. A. M. *et al.* Procedure for measuring electrical resistivity of anisotropic materials: A revision of the Montgomery method. *Journal of Applied Physics* **110**, 083703, doi:10.1063/1.3652905 (2011).
- 61 Li, J. *et al.* Nematic superconducting state in iron pnictide superconductors. *Nature Communications* **8**, 1880, doi:10.1038/s41467-017-02016-y (2017).
- 62 Cao, Y. *et al.* Nematicity and competing orders in superconducting magic-angle graphene. *Science* **372**, 264-271, doi:10.1126/science.abc2836 (2021).
- 63 Lake, E., Patri, A. S. & Senthil, T. Pairing symmetry of twisted bilayer graphene: A phenomenological synthesis. *Physical Review B* **106**, 104506, doi:10.1103/PhysRevB.106.104506 (2022).
- 64 Tinkham, M. *Introduction to Superconductivity*. (Dover Publications, 2004).
- 65 Ishida, S. *et al.* Anisotropy of the In-Plane Resistivity of Underdoped $\text{Ba}(\text{Fe}_{1-x}\text{Co}_x)_2\text{As}_2$ Superconductors Induced by Impurity Scattering in the Antiferromagnetic Orthorhombic Phase. *Physical Review Letters* **110**, 207001, doi:10.1103/PhysRevLett.110.207001 (2013).
- 66 Rosenthal, E. P. *et al.* Visualization of electron nematicity and unidirectional antiferroic fluctuations at high temperatures in NaFeAs . *Nature Physics* **10**, 225-232, doi:10.1038/nphys2870 (2014).
- 67 Schmidt, J. *et al.* Nematicity in the superconducting mixed state of strain detwinned underdoped $\text{Ba}(\text{Fe}_{1-x}\text{Co}_x)_2\text{As}_2$. *Physical Review B* **99**, 064515, doi:10.1103/PhysRevB.99.064515 (2019).

Supplementary Material

To prepare single crystals of $\text{Ba}(\text{Fe}_{1-x}\text{M}_x)_2\text{As}_2$, the flux and Barium were mixed with a ratio of $\text{Ba}:\text{Fe}_{1-x}\text{M}_x\text{As} = 1:4.5$ in an Al_2O_3 crucible and sealed under vacuum in a quartz tube. The tube was first warmed up to 900°C over 20 hours, then to 1175°C for 10 hours, cooled to 1050°C in 25 hours, and lastly left to cool to room temperature with the furnace off. The underdoped samples were grown using Ni with $x = 0.04$, while the overdoped samples were grown using Co with $x = 0.11$. Larger crystals were aligned and later cut along the orthorhombic a and b axes into roughly $2 \times 2 \text{ mm}^2$ squares using a Laue x-ray diffractometer and a wire saw respectively. Samples were then detwinned via uniaxial pressure with a small brass clamp [Fig. S3].

Two additional overdoped samples were measured nearer to the optimal doping to demonstrate no/negligible anisotropy in the overdoped regime. Figure S4(a) shows an analogous plot to Fig. 2 only with an overdoped sample with $\sim 7\%$ Co-content. Figures S4(b) and S4(c) are analogous plots to Fig. 3, but with nearly optimal doping $\sim 6.5\%$. Figure S5 shows resistivity across superconducting transition. Figure S6 shows normal state field dependence resistivity. Both Figs. 5 and 6 are for $\text{Ba}(\text{Fe}_{1-x}\text{Ni}_x)_2\text{As}_2$ with $x \sim 0.04$ sample. Figure S7 shows in-plane magnetic field dependence magnetoresistance in the normal state at 18 K, which is small and has no in-plane field directional dependence.

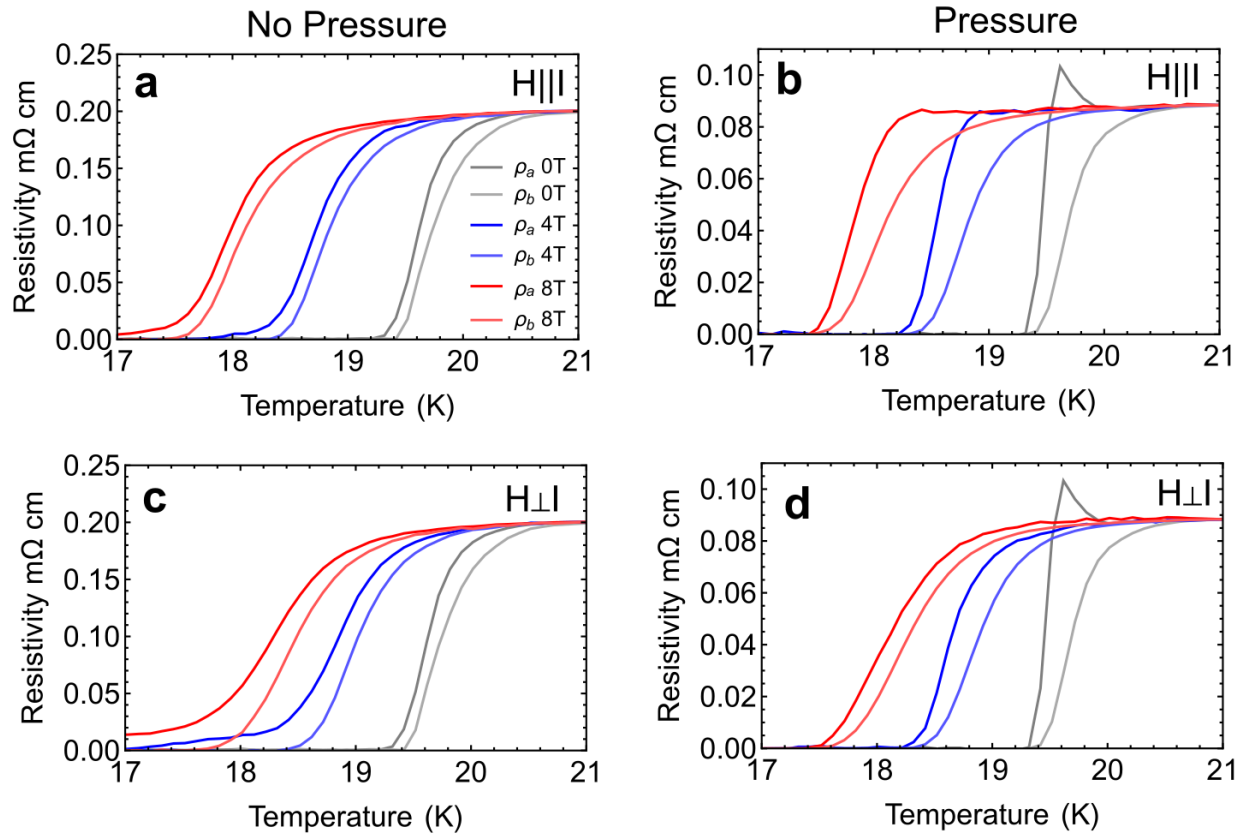


Fig. S1: (a) In-plane resistivity anisotropy with the field aligned along the current direction in the absence of strain. (b) With strain applied, the in-plane resistivity anisotropy with the field aligned along the current direction. (c) and (d) are the analogs to (a) and (b), respectively, with the field now aligned perpendicularly to the current.

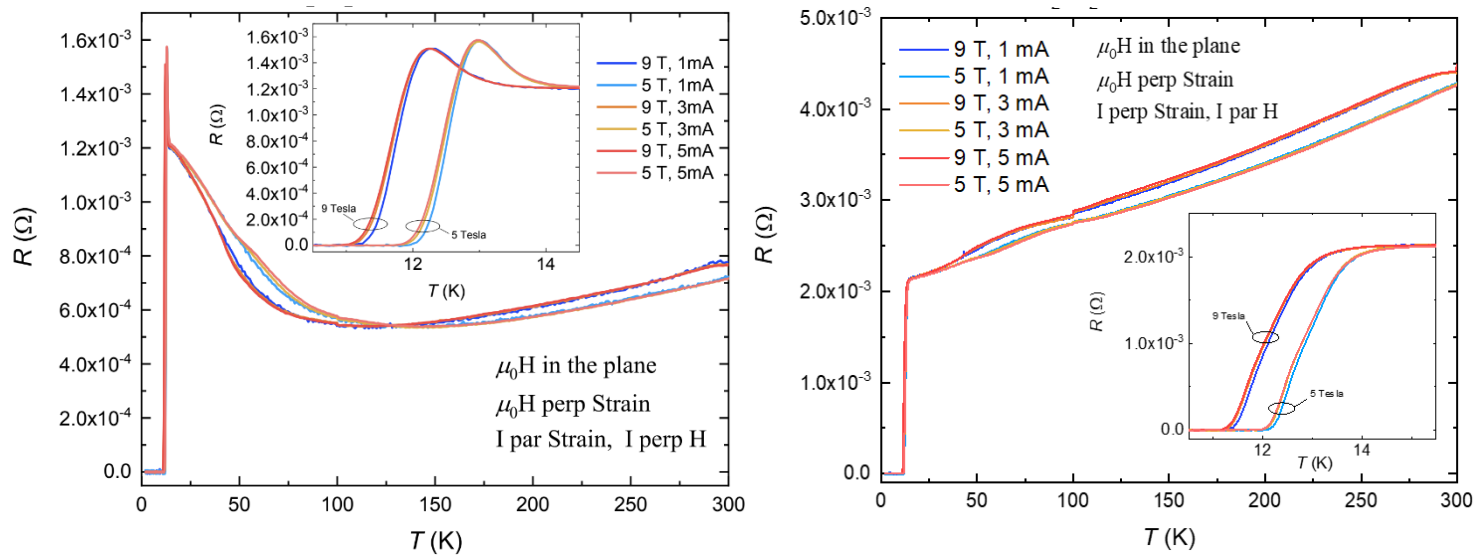


Fig. S2: Current dependence of the resistance of an underdoped sample showing resistivity along b (left) and a (right) axes. Three different currents (1, 3, & 5 mA) were measured at two fields (5,9 T). Inset highlights the temperature region immediately surrounding T_c .

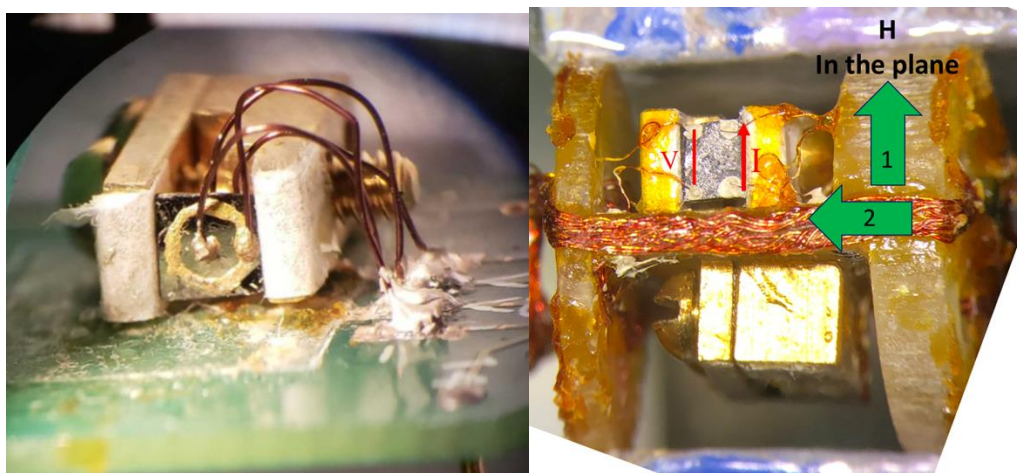


Fig. S3: Single crystal mounted on a brass clamp and wired in a Corbino geometry mounted on a Physical Property Measurements System puck (left). Two single crystals in two brass clamps mounted for measurements at the MagLab, with a diagram depicting voltage and current configuration for ρ_a (right).

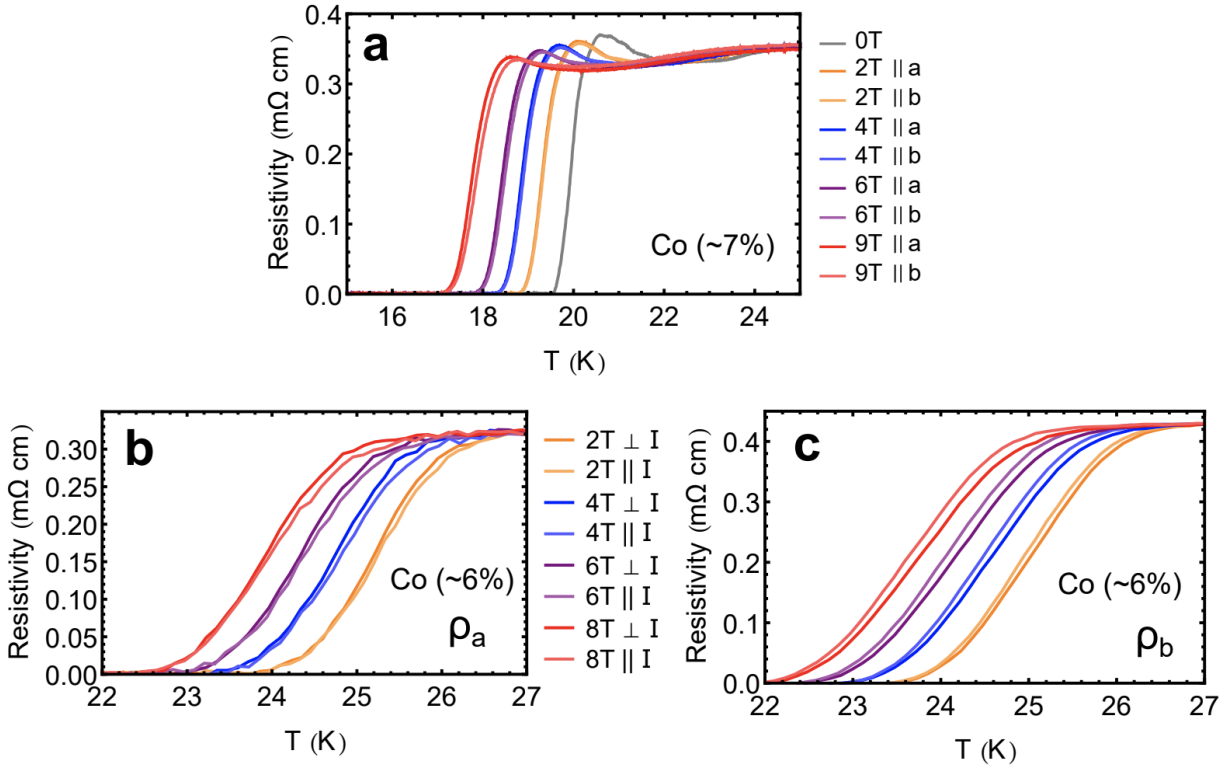


Fig. S4: (a) Overdoped sample measured with current along the c -axis using a Corbino geometry with roughly 7% Co-doping. (b,c) Resistivity ρ_a and ρ_b , respectively, as a function of temperature for distinct orientations of the current relative to field for a different overdoped sample, close to optimally doped ~6% Co.

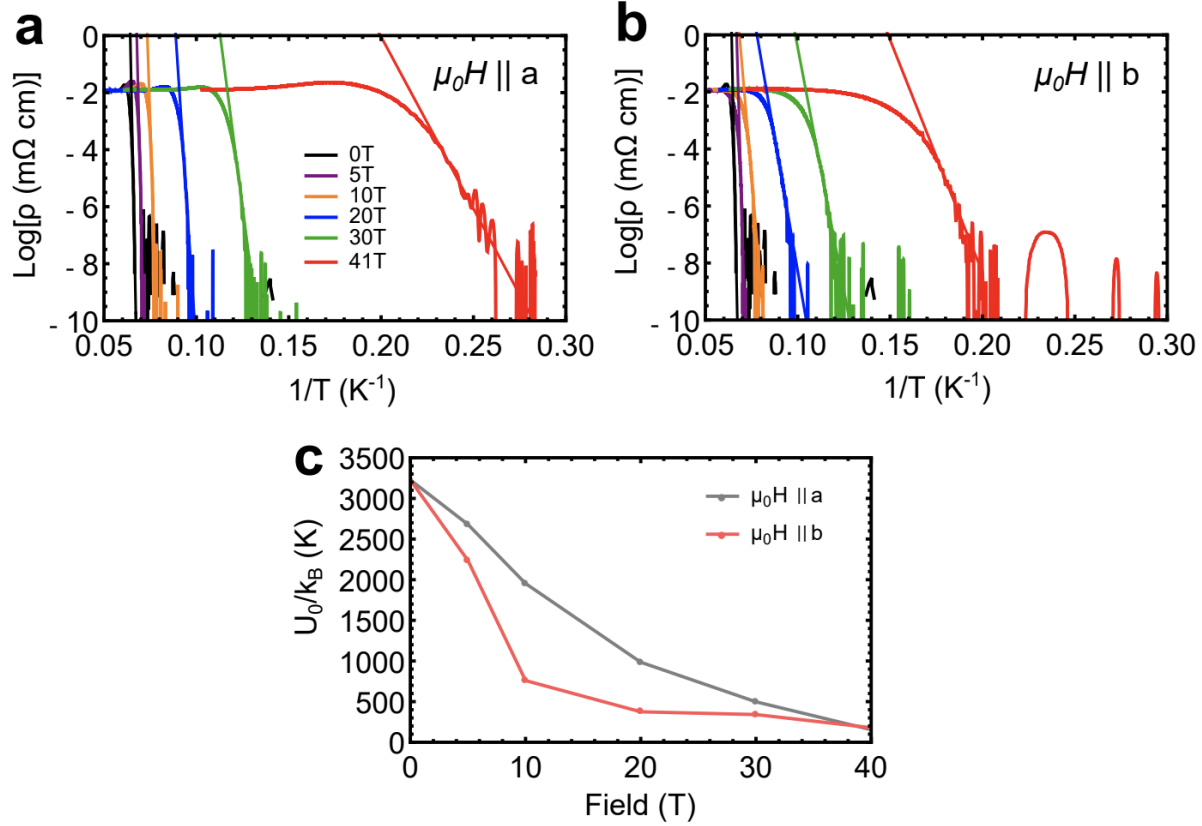


Fig. S5: (a) Resistivity across the superconducting transition in a logarithmic scale and for fields along the a -axis, as a function of the inverse temperature. Straight lines are linear fits from which we extract the activation energy U_0 for vortex flow. (b) Same as in (a) but for fields along the b -axis. (c) U_0/k_B as a function of magnetic field for both field orientations.

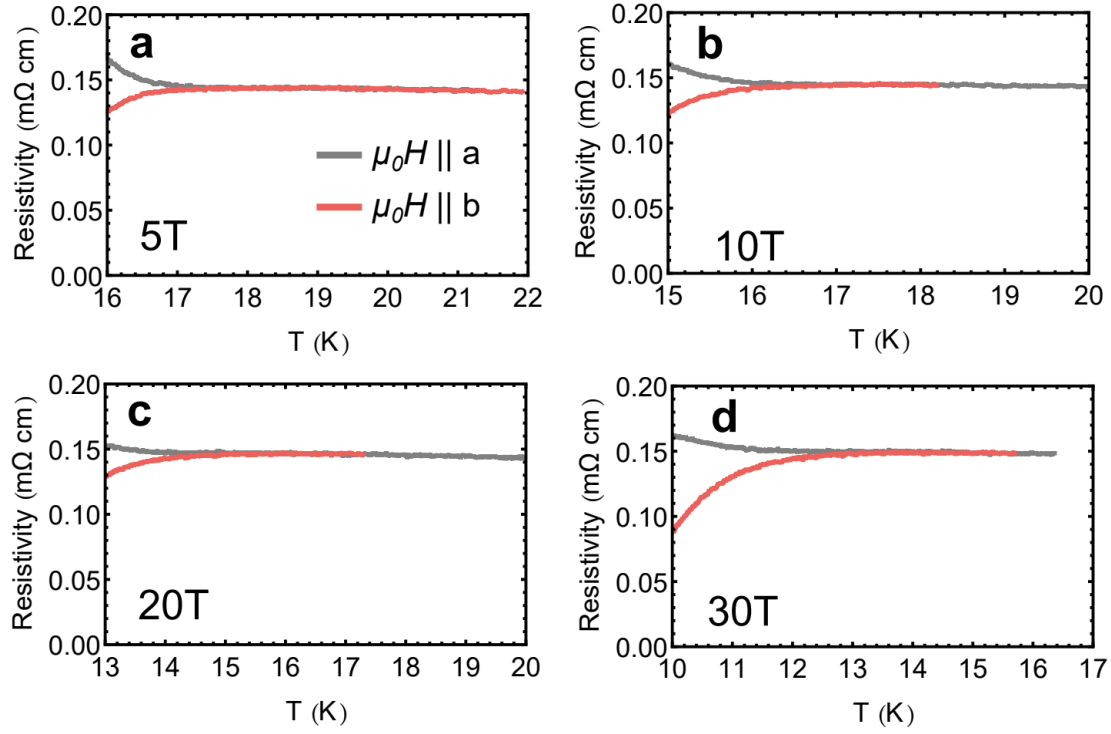


Fig. S6: (a-d) Field directional dependence of the normal state resistivity at 5, 10, 20, and 30 T. Data in this figure is the same as in Fig. 2(a,c,e) and is presented without scaling. This plot excludes data under $\mu_0 H = 41$ T since there is minimal overlap of the normal state resistivities.

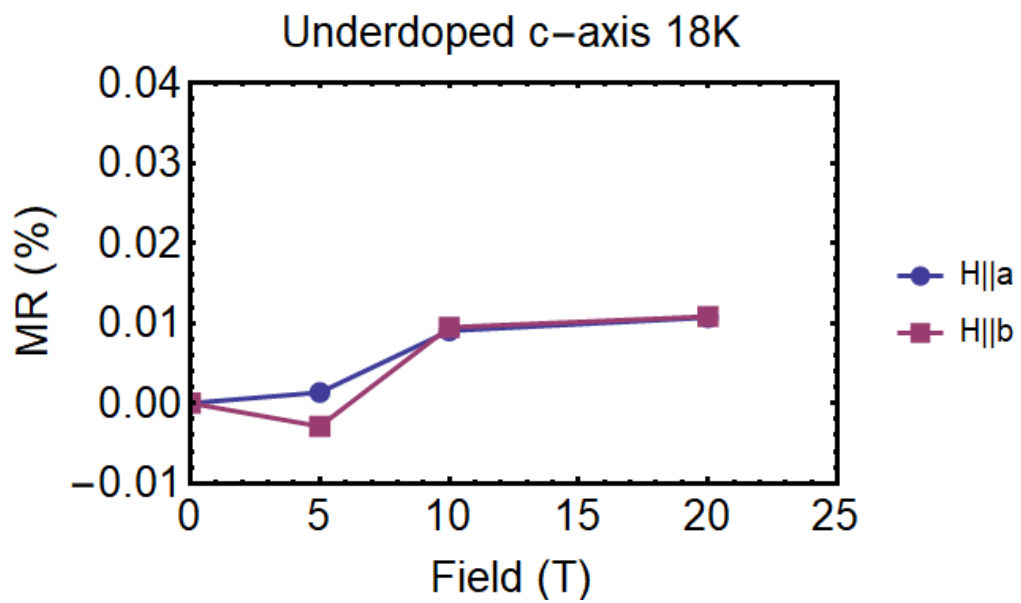


Fig. S7: Magnetoresistance (MR) of the underdoped crystal measured with *c*-axis resistivity and fields along the *a* and *b* axes from Fig. 2(a,c,e). The MR is negligible at 1% of 1% and the sample exhibits no in-plane directional field dependence.